

Ising-type quantum spin liquid state in $\text{PrMgAl}_{11}\text{O}_{19}$

N. Li,^{1,*} A. Rutherford,^{2,*} Y. Y. Wang,¹ H. Liang,¹ Q. J. Li,³ Z. J. Zhang,⁴ H. Wang,⁵ W. Xie,⁵ H. D. Zhou,^{2,†} and X. F. Sun^{1,‡}

¹*Anhui Key Laboratory of Magnetic Functional Materials and Devices,
Institutes of Physical Science and Information Technology,
Anhui University, Hefei, Anhui 230601, People's Republic of China*

²*Department of Physics and Astronomy, University of Tennessee, Knoxville, Tennessee 37996, USA*

³*School of Physics and Optoelectronics, Anhui University,
Hefei, Anhui 230061, People's Republic of China*

⁴*School of Information & Electronic Engineering (Sussex Artificial Intelligence Institute),
Zhejiang Gongshang University, Hangzhou, Zhejiang 310018, People's Republic of China*

⁵*Department of Chemistry, Michigan State University, East Lansing, Michigan 48824, United States*
(Dated: July 17, 2024)

We have grown single crystals of $\text{PrMgAl}_{11}\text{O}_{19}$, an ideal triangular-lattice antiferromagnet, and performed magnetic susceptibility, specific heat and thermal conductivity measurements at low temperatures. The main results are as follows: (i) The temperature-dependent susceptibility shows a negligible in-plane response and the isothermal magnetization curves confirm the easy axis along the c axis. (ii) The specific heat measurements reveal the absence of long-range magnetic order down to 60 mK, and the power-law temperature dependence indicates the existence of the gapless magnetic excitations in system. (iii) The ultralow-temperature thermal conductivity exhibits negligibly small residual term (κ_0/T) and strong spin-phonon scattering effect, suggesting that the spin excitations are also involved. Our results further demonstrate that $\text{PrMgAl}_{11}\text{O}_{19}$ is a rare quantum spin liquid candidate with Ising-like anisotropy.

I. INTRODUCTION

The strong frustration effect in antiferromagnets leads to strong quantum fluctuations that prevent the formation of long-range magnetic order. These systems have rich and exotic quantum magnetisms, quantum phase transition behaviors, and peculiar elementary excitations [1]. In fact, the most striking physical state is the quantum spin liquid (QSL), in which the strongly interacted spins do not develop a conventional long-range magnetic order even at the absolute zero-temperature limit, but highly correlate with each other due to long-range quantum entanglement. Moreover, QSLs have some special elementary excitations, including spinons, Majorana fermions and topological visons, which are closely related to quantum information, quantum computing and high temperature superconductivity. Therefore, QSL has attracted extensive attentions and become one of the focuses in condensed matter physics [2–4].

In 1973, Anderson first proposed the resonating valence bond (RVB) model to describe this novel quantum disorder state based on Heisenberg antiferromagnets with two-dimensional triangular lattices [5]. Since then, many efforts have been devoted to realizing this exotic quantum disorder state in real materials, especially in low-dimensional antiferromagnetically correlated systems with small spin quantum numbers or strong frustration effects. Typical research systems

are two-dimensional triangular lattice and kagome lattice, three-dimensional pyrochlore lattice, and more recently, two-dimensional honeycomb lattice. Among them, the triangular-lattice is the most representative system, in which the organic antiferromagnets κ -(BEDTTTF)₂Cu₂(CN)₃ and EtMe₃Sb[Pd(dmit)₂]₂ with $S = 1/2$ were identified as QSL candidates [6, 7]. For inorganic materials, some new QSL candidates have also emerged, including YbMgGaO₄, ARCh_2 (A = alkali or monovalent ions, R = rare earth ions, Ch = chalcogenides), Na₂BaCo(PO₄)₂, $\text{PrMAl}_{11}\text{O}_{19}$ (M = Zn, Mg), NdTa₇O₁₉, Ba₆R₂Ti₄O₁₇ (R = rare earth ions), YbZn₂GaO₅, NaRuO₂, TbInO₃ etc [8–17].

The inevitable disorder effects such as vacancies, impurities, lattice distortion, and stacking faults in real materials often cause many controversies in QSL candidates. The canonical examples including the kagome-lattice system Zn₃Cu(OH)₆Cl₂ and the triangular-lattice ytterbium-based compound YbMgGaO₄. For Zn₃Cu(OH)₆Cl₂, it has been confirmed that about 5 ~ 15 % of magnetic Cu²⁺ ions on the interlayer sites occupied by non-magnetic Zn²⁺ ions, and this structural disorder may affect the magnetic exchange interactions significantly [18, 19]. Therefore, it is difficult to accurately characterize the real ground state in theory and experiments. However, unlike the case of Zn₃Cu(OH)₆Cl₂, there is a site mixing between nonmagnetic Mg²⁺ and Ga³⁺ ions in YbMgGaO₄, causing the controversy on the ground state and the low-energy magnetic excitations [20–22]. Consequently, there is an urgent need for an almost ideal system to better investigate the QSL states.

Recently, it has been reported that $\text{PrMAl}_{11}\text{O}_{19}$ (M = Zn, Mg) is a promising QSL candidate with perfect two-

* These authors contributed equally to this work.

† hzhou10@utk.edu

‡ xfsun@ahu.edu.cn

dimensional triangular-lattice with only a weak disorder between nonmagnetic M^{2+} and Al^{3+} ions, which has a negligible effect on the ground state [23, 24]. Previous studies indicated the absence of long-range magnetic order at ultralow temperatures, and the results of specific heat and inelastic neutron scattering revealed the existence of gapless low-energy excitations, in favor of the possible gapless QSL in $\text{PrMgAl}_{11}\text{O}_{19}$ ($M = \text{Zn}, \text{Mg}$). In particular, the recent work claimed that $\text{PrMgAl}_{11}\text{O}_{19}$ is likely a rare Ising-antiferromagnet exhibiting gapless QSL [23].

In this work, we have grown high-quality $\text{PrMgAl}_{11}\text{O}_{19}$ single crystal and have systematically studied its magnetic properties, specific heat and thermal conductivity at low temperatures. The results indicate no sign of long-range magnetic order at low temperatures down to several tens of milliKelvin. The temperature-dependent susceptibility and the isothermal magnetization indicate Ising-like anisotropy with easy axis along the c axis. The negative Curie-Weiss temperature obtained from the magnetic susceptibility shows the dominant anti-ferromagnetic interactions between Pr^{3+} ions. A clear power-law temperature dependence is observed on the low-temperature specific heat, suggesting the existence of gapless spinon excitations. Besides, the main experimental result of present work is that the ultralow temperature thermal conductivity displays a rough T^2 dependence and a negligibly small residual term κ_0/T . It indicates the strong spin-phonon scattering and therefore the existence of spinons at ultralow temperatures. Our results further verify the realization of Ising-like QSL in $\text{PrMgAl}_{11}\text{O}_{19}$.

II. EXPERIMENTS

$\text{PrMgAl}_{11}\text{O}_{19}$ single crystals were grown using the floating zone method. The feed and seed rods for the crystal growth were prepared by solid state reactions. The stoichiometric mixtures of Pr_6O_{11} (pre-dried at 1000 °C for overnight), MgO , and Al_2O_3 were ground together and pressed into 6-mm-diameter 60-mm rods under 400-atm hydrostatic pressure and then calcined in air at 1000 °C for 20 hours and at 1400 °C for 20 hours, and finally in argon at 1400 °C for 20 hours with intermediate grindings. The crystal growth was carried out in argon in an IR-heated image furnace equipped with two halogen lamps and double ellipsoidal mirrors with feed and seed rods rotating in opposite directions at 20 rpm during crystal growth at a rate of 2.0 mm/hour. The obtained $\text{PrMgAl}_{11}\text{O}_{19}$ single crystal with size of several centimeters is shown in Fig. 1(b). The Laue back diffraction measurement was used to determine the crystalline orientation. The single crystal X-ray diffraction (SCXRD) measurement was performed using a XtalLAB Synergy, Dualflex, Hypix single crystal X-ray diffractometer with Mo K_α radiation ($\lambda = 0.71073$ Å). The structure was solved and refined using the Bruker SHELXTL Software

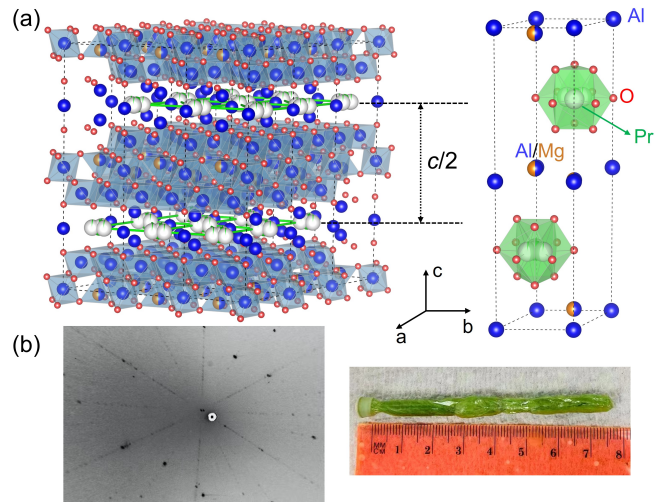


FIG. 1. (a) The schematic crystal structure of $\text{PrMgAl}_{11}\text{O}_{19}$, where Pr^{3+} ions form into an ideal triangular layer in the ab plane and these triangular layers are stacked along the c axis with the nearest-neighbor interlayer distance of 10.9558 Å. (b) The X-ray Laue back diffraction photo for the ab plane and the photograph of $\text{PrMgAl}_{11}\text{O}_{19}$ single crystal grown by using the optical floating-zone technique.

Package.

The dc magnetic susceptibility between 2 and 300 K were measured using the SQUID-VSM (Quantum Design Magnetic Property Measurement System, MPMS) in magnetic field up to 7 T. The dc magnetization up to 14 T was measured using a VSM equipped with the Physical Property Measurement System (PPMS) (DynaCool, Quantum Design). The specific heat was measured by relaxation technique using PPMS with a dilution insert. The same sample was used for both magnetic properties and specific heat measurements. The $\text{PrMgAl}_{11}\text{O}_{19}$ single crystal for thermal conductivity measurements was cut precisely along the a axis with dimension of $2.5 \times 0.64 \times 0.16$ mm³ after being oriented by using the X-ray Laue system. The thermal conductivity was measured by using “one heater, two thermometers” technique in a dilution refrigerator (70 mK to 1 K) and a ^3He refrigerator (0.3 to 30 K) equipped with a 14 T magnet [25–27]. The heat current was along the longest direction (a axis) and the external magnetic fields were applied along either the a or c axis. It should be pointed out that $\text{PrMgAl}_{11}\text{O}_{19}$ single crystal is so easily cleaved along the ab plane that it is not possible to cut a long-bar shaped sample along the c axis.

III. RESULTS AND DISCUSSION

A. Crystal structure

The crystalline structure of as-grown $\text{PrMgAl}_{11}\text{O}_{19}$ crystal is determined by the SCXRD data refinement

TABLE I. The crystal structure and refinement for $\text{PrMgAl}_{11}\text{O}_{19}$ at 300 K.

Chemical Formula	$\text{PrMgAl}_{11}\text{O}_{19}$
Formula weight	766.00 g/mol
Space Group	$P6_3/mmc$
Unit cell dimensions	$a = 5.58865(6) \text{ \AA}$ $c = 21.9115(4) \text{ \AA}$
Volume	$592.675(16) \text{ \AA}^3$
Density(calculated)	4.292 g/cm^3
Extinction coefficient	$0.0234(10)$
Absorption coefficient	5.130 mm^{-1}
F(000)	732
2θ range	7.44 to 80.84°
Total Reflections	17535
Independent reflections	782 [$R_{\text{int}} = 0.0356$]
Refinement method	Full-matrix least-squares on F^2
Data/restraints/parameters	782 / 0 / 48
Final R indices	$R_1 (I > 2\sigma(I)) = 0.0145$; $wR_2 (I > 2\sigma(I)) = 0.0389$ $R_1(\text{all}) = 0.0150$; $wR_2(\text{all}) = 0.0391$
Largest diff. peak and hole	$+0.969 \text{ e/\AA}^{-3}$ and $-1.485 \text{ e/\AA}^{-3}$
R.M.S. deviation from mean	0.124 e/\AA^{-3}
Goodness-of-fit on F^2	1.127

TABLE II. Atomic coordinates and equivalent isotropic atomic displacement parameters (\AA^2). (U_{eq} is defined as one third of the trace of the orthogonalized U_{ij} tensor.)

$\text{PrMgAl}_{11}\text{O}_{19}$	Wyck.	x	y	z	Occ.	U_{eq}
Pr ₁	2d	0.333333	0.666667	0.750000	0.900(2)	0.00828(7)
Pr ₂	6h	0.4650(16)	0.7325(8)	0.750000	0.0174(8)	0.0096(17)
Al ₁	2a	0	0	0	1	0.00420(12)
Al ₂	2b	0	0	0.750000	1	0.0214(3)
Al ₃	4f	0.666667	0.333333	0.81007(3)	1	0.00419(10)
Al ₄	4f	0.333333	0.666667	0.02729(3)	0.500	0.00399(11)
Al ₅	12k	0.16749(3)	0.33497(6)	0.89165(2)	1	0.00434(8)
Mg	4f	0.333333	0.666667	0.94194(6)	0.5	0.00399(11)
O ₁	4e	0	0	0.84850(6)	1	0.00565(18)
O ₂	4f	0.333333	0.666667	0.94194(6)	1	0.00583(19)
O ₃	6h	0.81874(11)	0.18126(11)	0.750000	1	0.00721(16)
O ₄	12k	0.01073(14)	0.50536(7)	0.84843(3)	1	0.00533(12)
O ₅	12k	0.69510(16)	0.84755(8)	0.05368(3)	1	0.00718(12)

with a $P6_3/mmc$ space group. The obtained lattice parameters and atomic coordinates are summarized in Tables I and II. The schematic crystal structure of $\text{PrMgAl}_{11}\text{O}_{19}$ is shown in Fig. 1(a). The magnetic Pr^{3+} ion is coordinated within a PrO_{12} tetrakaidecahedron and form an ideal triangular-lattice layer with the nearest-neighbor Pr-Pr intra-layer distance of $a = 5.58865(6) \text{ \AA}$. These triangular-lattice layers are stacked along the c axis with $c = 21.9115(4) \text{ \AA}$, separated by nonmagnetic AlO_6 octahedra and $(\text{Mg}, \text{Al})\text{O}_4$ tetrahedra, which indicates a quasi-two-dimensional structural characteristic of $\text{PrMgAl}_{11}\text{O}_{19}$. Due to the large ion radius difference between magnetic (Pr^{3+}) and nonmagnetic ($\text{Mg}^{2+}/\text{Al}^{3+}$) ions, the site mixing disorder is eliminated. The obtained green crystal is easy to cleave along the ab plane and this orientation was confirmed by Laue back diffraction pattern (Fig. 1(b)).

B. Magnetic Properties

Magnetic susceptibility $\chi(T)$ measurements were performed from 2 to 300 K under different magnetic fields along the c or a axis, as shown in Figs. 2(a) and Fig. 2(c). The absence of any anomaly in $\chi(T)$ curves indicates that the Pr^{3+} moments do not undergo a long range magnetic ordering down to 2 K. The absence of splitting of $\chi(T)$ between zero field cooling (ZFC) and field cooling (FC) under 0.1 T precludes spin freezing. Due to the presence of crystal electric field (CEF) effect, the $\chi(T)$ curves deviate the Curie-Weiss (CW) behavior at the intermediate temperature. The low-temperature (2 – 20 K) CW fittings to the 0.1 T data yield $\theta_{\text{CW}} = -8.44 \text{ K}$, $\mu_{\text{eff}} = 5.0 \mu_{\text{B}}/\text{Pr}$ and $\theta_{\text{CW}} = -24.85 \text{ K}$, $\mu_{\text{eff}} = 1.39 \mu_{\text{B}}/\text{Pr}$ for $B \parallel c$ and $B \parallel a$, respectively. The negative θ_{CW} reveals dominant antiferromagnetic exchange interaction between Pr^{3+} ions. For $B \parallel c$, the magnetic sus-

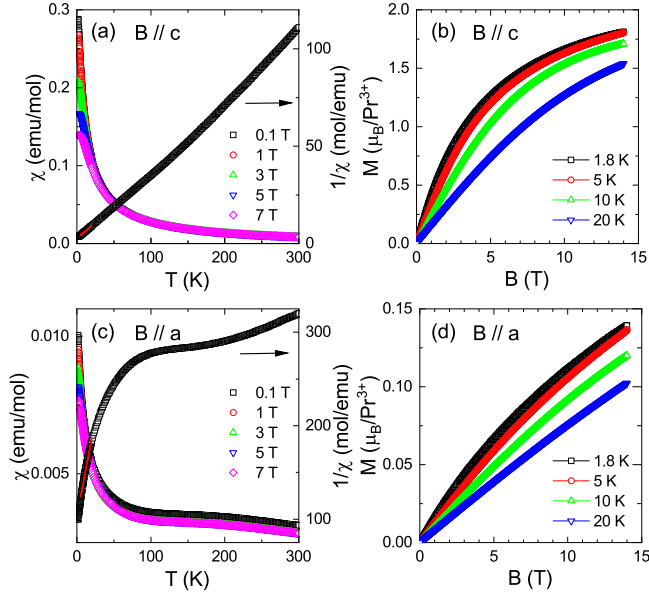


FIG. 2. (a, c) Temperature dependence of dc magnetic susceptibility and the inverse magnetic susceptibility with external magnetic fields along the c or a axis. The solid red lines indicate the CW fitting at $2 \leq T \leq 20$ K under $B = 0.1$ T. (b, d) Magnetic field dependence of the magnetization at selected temperatures with $B \parallel c$ and $B \parallel a$, respectively.

ceptibility at high temperatures are almost independent on the external magnetic field, while the susceptibility at low temperatures gradually decreases with increasing magnetic field. In contrast, for $B \parallel a$, the magnetic susceptibility is two orders of magnitude smaller compared with $B \parallel c$, and the magnetic susceptibility gradually reduces with increasing magnetic field, which suggests the Ising-like anisotropy in $\text{PrMgAl}_{11}\text{O}_{19}$ [28].

The isothermal field-dependent magnetization curves $M(B)$ at selected temperatures are shown in Figs. 2(b) and 2(d) for $B \parallel c$ and $B \parallel a$, respectively. At these temperatures, the $M(B)$ curves exhibit nonlinear field dependence without magnetic saturation up to 14 T for both directions, and the maximum magnetization value is about $1.79 \mu_B/\text{Pr}^{3+}$ and $0.14 \mu_B/\text{Pr}^{3+}$, respectively, much smaller than the theoretical saturation value of $3.58 \mu_B/\text{Pr}^{3+}$ for free ions. These data further indicate large spin anisotropy with easy axis along the c axis.

To detect the low-energy excitations of $\text{PrMgAl}_{11}\text{O}_{19}$ single crystal, we perform the specific heat measurements from 60 mK to 30 K with $B \parallel c$, and the temperature dependence of specific heat $C_p(T)$ curves are shown in Fig. 3. It can be seen that there is no sharp λ -shape anomaly down to several tens of milliKelvin, indicating the absence of long-range magnetic order of Pr^{3+} ions despite of the presence of a large AFM interaction ($\theta_{\text{CW}} = -8.44$ K), which may imply the possible realization of the QSL state. Noted that the lowest-temperature upturns of $C_p(T)$ is related to the nuclear Schottky anomaly, which shifts to higher temperature with increasing magnetic

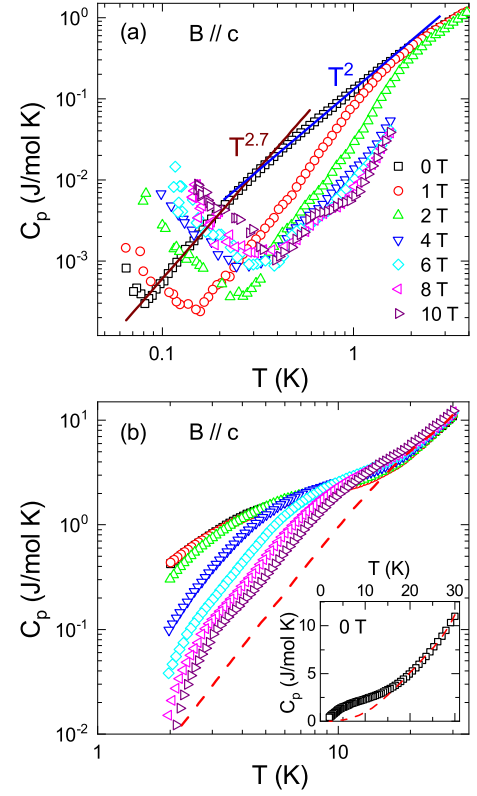


FIG. 3. (a) Ultralow-temperature specific heat $C_p(T)$ of $\text{PrMgAl}_{11}\text{O}_{19}$ single crystal under different magnetic fields along the c axis. The solid lines indicate the $T^{2.7}$ and T^2 dependence, respectively. (b) The temperature dependence of specific heat with external magnetic fields along the c axis at $2 < T < 30$ K. Inset: the zero-field specific heat data. The dashed lines show the fitting to the high- T data by using the formula of phonon specific heat $C = \beta T^3 + \beta_5 T^5 + \beta_7 T^7$.

field. Moreover, the zero-field $C_p(T)$ curve exhibits a hump around 4 K indicative of low-lying crystal field excitations, which is commonly observed in some rare-earth-based frustrated triangular-lattice antiferromagnets [29–32]. The hump is gradually suppressed and shifts to higher temperatures with increasing external magnetic field, as shown in Fig. 3(b).

With increasing magnetic field, the low-temperature specific heat is significantly decreased, besides the lowest-temperature upturn of the nuclear Schottky term. This indicates that at zero field the low-temperature specific heat is dominated by the magnetic excitations while the phonon term is negligibly small. As we can see that the specific heat obeys the $T^{2.7}$ and T^2 power-law temperature dependence at $80 \text{ mK} < T < 300 \text{ mK}$ and $300 \text{ mK} < T < 2 \text{ K}$, respectively. Although the power exponent is sensitive to the fitting temperature range, which is similar to kagome compound $\text{ZnCu}_3(\text{OH})_6\text{Cl}_2$, it still may evidence the gapless magnetic excitations [33]. In fact, this power-law temperature dependence has already been reported in some QSL candidates as one of the experimental hallmarks for gapless low-energy

magnetic excitations, such as the triangular-lattice compound YbMgGaO_4 and $\text{YbZn}_2\text{GaO}_5$ [8, 15], the kagome-lattice compound $\text{YCu}_3(\text{OH})_{6+x}\text{Br}_{3-x}$ ($x \approx 0.5$) and $\text{ZnCu}_3(\text{OH})_6\text{Cl}_2$ [32–34]. In particular, the sister material $\text{PrZnAl}_{11}\text{O}_{19}$ also shows exhibits a $T^{1.897}$ behavior of zero-field magnetic specific heat at $\sim 0.3 - 3$ K and some slope change at lower temperatures (the measurement was done only down to 200 mK) [24]. Furthermore, the recent study on $\text{PrMgAl}_{11}\text{O}_{19}$ also revealed a T^2 behavior of zero-field magnetic specific heat at $\sim 0.3 - 1$ K, as well as a different temperature dependence at lower temperatures [23].

We have done quantitative analysis on phonon contribution of the specific heat. It is known that in the temperature range $0.02 < T/\Theta_D < 0.1$ (Θ_D is the Debye temperature), one can use the low-frequency expansion of the Debye function, $C = \beta T^3 + \beta_5 T^5 + \beta_7 T^7$, where β , β_5 and β_7 are temperature-independent coefficients [35, 36]. As shown in Fig. 3(b), the fitting to the zero-field data at relatively high temperatures yields parameters $\beta = 1.09 \times 10^{-3} \text{ J/K}^4\text{mol}$, $\beta_5 = -1.43 \times 10^{-6} \text{ J/K}^6\text{mol}$ and $\beta_7 = 7.60 \times 10^{-10} \text{ J/K}^8\text{mol}$. At very low temperatures, the T^5 - and T^7 - terms are negligible and the phonon specific heat shows a well-known T^3 dependence with the coefficient of β . Note that this fitting result also indicates that the phonon specific heat is negligibly small at low temperatures.

C. Thermal conductivity

Figure 4 shows the low-temperature thermal conductivity of $\text{PrMgAl}_{11}\text{O}_{19}$ single crystal in zero and in 14 T magnetic field along the a or c axis. At zero field, the $\kappa(T)$ curve exhibits a rough T^2 -dependence at $70 \text{ mK} < T < 600 \text{ mK}$, as shown in Fig. 4(a), which significantly deviates from the standard T^3 behavior of phonon thermal conductivity at very low temperatures. It usually suggests that the phonons are strongly scattered with magnetic excitations [37]. When a 14 T magnetic field is applied along the a axis, the κ increases slightly at low temperature ($70 \text{ mK} < T < 1 \text{ K}$) and almost overlaps with the κ for $B = 0 \text{ T}$ at higher temperatures. In contrast, the κ is significantly enhanced and displays a stronger $T^{2.4}$ -dependence for $14 \text{ T} \parallel c$. This indicates that the magnetic scattering on phonon is strongly smeared out under the 14 T magnetic field along the c axis. It can be seen that the different responses of the κ for $B \parallel c$ and $B \parallel a$ further verify the Ising-like properties of $\text{PrMgAl}_{11}\text{O}_{19}$. That is, since the spin system is Ising-like with the easy axis along the c axis, even such a quite strong field along the a axis can hardly affect the spin system or spin excitations, whereas the 14 T along the c axis seems to strongly suppress the QSL phase and its spinon excitations.

It is possible to estimate the mean free path of phonons at low temperatures if the κ is mainly contributed by the phonons. The phononic thermal conductivity can be ex-

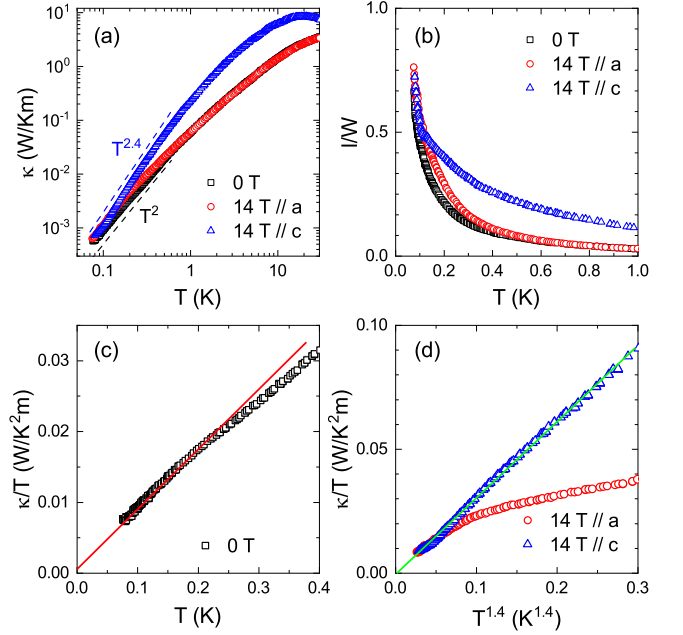


FIG. 4. (a) Temperature dependence of the a -axis thermal conductivity $\kappa(T)$ of $\text{PrMgAl}_{11}\text{O}_{19}$ single crystal under zero field and 14 T magnetic field applied along either the a or c axis, the dashed lines indicate the T^2 - and $T^{2.4}$ -behavior at zero field and 14 T magnetic field applied along the c axis, respectively. (b) Temperature dependence of the phonon mean free path l divided by the averaged sample width W . (c) The κ/T plotted as a function of T for ultralow temperature data at zero field. The solid line is the linear fitting of the data at $T < 200 \text{ mK}$ by using the formula $\kappa/T = \kappa_0/T + bT$, with a negligibly small residual thermal conductivity κ_0/T . (d) The κ/T plotted as a function of $T^{1.4}$ for $T < 420 \text{ mK}$ at 14 field along the a or c axis. The solid line is the linear fitting to the c -axis-field data with zero κ_0/T . The a -axis-field data also point to a vanishing κ_0/T .

pressed by the kinetic formula $\kappa_{ph} = \frac{1}{3} C v_p l$ [37], where $C = \beta T^3$ is phonon specific heat at low temperatures, v_p is the average velocity and l is the mean free path of phonon. Here $\beta = 1.09 \times 10^{-3} \text{ J/K}^4\text{mol}$ is obtained from the zero-field specific-heat data and $v_p = 2710 \text{ m/s}$ can be estimated from Debye temperature Θ_D using the relations $\beta = \frac{12\pi^4}{5} \frac{R_s}{\Theta_D^3}$ and $\Theta_D = \frac{\hbar v_p}{k_B} \left(\frac{6\pi^2 N_s}{V} \right)^{\frac{1}{3}}$ [35], where N is the number of molecules per mole and each molecule comprises s atoms, V is the volume of crystal and R the universal gas constant. Figure 4(b) shows the ratio of calculated l to the averaged sample width $W = 2\sqrt{A/\pi} = 0.367 \text{ mm}$ [37, 38], where A is the area of cross section. It can be seen that the ratio l/W increases with lowering temperature and becomes close to one at the lowest temperature, which means that the boundary scattering limit is nearly established at such low temperatures. It should be noted that these phonon mean free paths would be over-estimated if there were sizeable contribution to κ from other heat carriers.

Ultralow-temperature thermal conductivity is an effec-

tive tool to detect the characteristics of magnetic excitations in the system. Usually, one can use the formula $\kappa/T = \kappa_0/T + bT^{\alpha-1}$ to fit the thermal conductivity of insulator, where κ_0/T represents a constant contribution from gapless fermionic excitations and bT^α represents the phonon thermal conductivity with the exponent $\alpha = 2 \sim 3$ [25, 38]. For the zero-field data plotted as κ/T vs T , as shown in Fig. 4(c), the linear fitting at $T < 200$ mK gives an almost zero residual thermal conductivity, κ_0/T . Moreover, the larger κ in high fields indicates that, in zero magnetic field, the phonons are rather strongly scattered by magnetic excitations that are gapped out in high magnetic fields. Therefore, the absence of magnetic excitations in the thermal conductivity result at zero magnetic field is due to the spin-phonon scattering that not only weakens the phonon transport but also prevents the spinon transport. In this regard, it seems to be consistent with the recent neutron scattering measurements of $\text{PrMgAl}_{11}\text{O}_{19}$ that revealed the gapless spinon excitations [23].

For the data with $14 \text{ T} \parallel c$, since the temperature dependence is close to $T^{2.4}$, we can have a rather good linear fitting in the κ/T vs $T^{1.4}$ plot at $T < 420$ mK, which also gives a zero residual term, as shown in Fig. 4(d). For the low-temperature data with $14 \text{ T} \parallel a$, which are slightly larger than those at zero field, they display some clear change of the temperature dependence at about 200 mK. Nevertheless, the lowest-temperature data with $14 \text{ T} \parallel a$ are very comparable to those at $14 \text{ T} \parallel c$ and therefore also point to a zero κ_0/T , as shown in Fig. 4(d). The absence of fermions contribution to the κ with applying strong magnetic field is always the case for QSL candidates, due to the suppression of QSL phase by magnetic field.

Figure 5 shows the magnetic field dependence of thermal conductivity at different temperatures with external magnetic field along the a or c axis. For $B \parallel a$, the $\kappa(B)/\kappa(0)$ isotherms display a weak increase ($\sim 30\%$) at $T = 151$ mK, while the magnetic-field dependence of κ weakens gradually with increasing temperature, as shown in Fig. 5(a). In contrast, the $\kappa(B)/\kappa(0)$ is significantly enhanced at high magnetic fields for $B \parallel c$, as shown in Fig. 5(b). At $T = 151$ mK, the $\kappa(B)/\kappa(0)$ quickly reaches saturation around $B = 1$ T, which means at such low temperature the spins are easily polarized by the c -axis magnetic field. In other word, the proposed QSL state and spinon excitations can be easily suppressed by the c -axis magnetic field. As the temperature increases, the saturated magnetic field in $\kappa(B)/\kappa(0)$ curve gradually increases, which is also compatible with the magnetization behavior shown in Fig. 2(b). At $T = 5$ K, the high-field enhancement of $\kappa(B)/\kappa(0)$ can be as high as 540 %, which clearly reveals the strong scattering between magnetic excitations and phonons at zero field. The above significant different field dependence of κ between $B \parallel c$ and $B \parallel a$ further demonstrates the strong spin anisotropy in $\text{PrMgAl}_{11}\text{O}_{19}$.

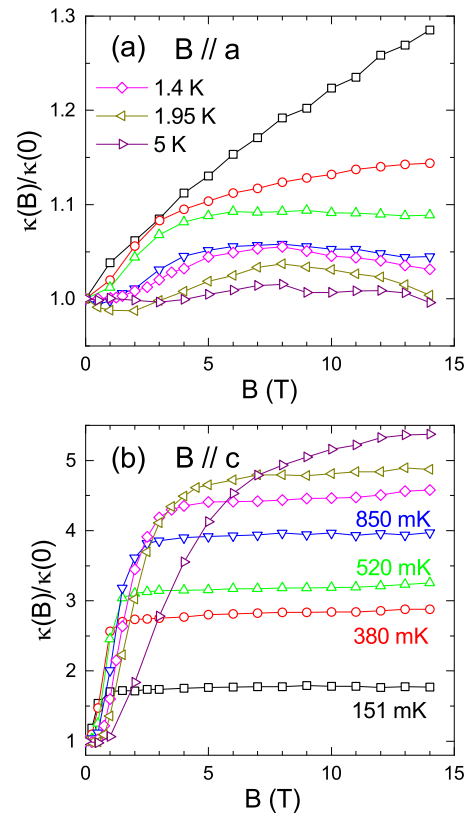


FIG. 5. The magnetic field dependence of thermal conductivity at different temperatures with external magnetic field along the a and c axis, respectively.

IV. DISCUSSION

In the exploration of the classification and ground state characteristics of QSL candidates, disorder plays an important role. Due to the large difference in the ionic radius of Pr^{3+} and $\text{Al}^{3+}/\text{Mg}^{2+}$ ions, the site mixing between magnetic and nonmagnetic ions is effectively avoided in $\text{PrMgAl}_{11}\text{O}_{19}$. But there is a weak site mixing between the nonmagnetic Al^{3+} and Mg^{2+} ions, as shown in Fig. 1(a), which is similar to the case of YbMgGaO_4 , in which nonmagnetic Ga^{3+} and Mg^{2+} ions randomly distribute [8, 11]. Since the occupation mixing only exists in Mg/AlO_4 tetrahedra with small proportion, the disorder in $\text{PrMgAl}_{11}\text{O}_{19}$ is much weaker compared with the case of YbMgGaO_4 [11, 23]. Moreover, the nearest-neighbor magnetic layers are separated by four layers of nonmagnetic $\text{Al}/\text{Mg-O}$ polyhedrons, the disorder effect should be negligible for the ground-state properties and all of our measurements reflect the intrinsic properties of $\text{PrMgAl}_{11}\text{O}_{19}$. Our magnetic susceptibility results differ by two orders of magnitude for $B \parallel c$ and $B \parallel a$, indicating the Ising-like characteristics, which is consistent with the results reported recently [23]. In addition, the specific heat indicates the absence of long-range magnetic order and the power-law temperature dependence of magnetic specific heat, which points to

a possible gapless QSL state. The spin dynamics results of $\text{PrMgAl}_{11}\text{O}_{19}$ are similar to its sister compound $\text{PrZnAl}_{11}\text{O}_{19}$, which has been claimed to possess a QSL with gapless spinon excitations [24]. Recently, the quasi-quadratic temperature-dependent behavior of magnetic specific heat has already been reported and a broad continuum of low-energy magnetic excitation spectra was captured by the inelastic neutron scattering technique at 55 mK, evidencing the possible realization of a gapless QSL state in $\text{PrMgAl}_{11}\text{O}_{19}$ [23].

Ultralow-temperature thermal conductivity has been proved to be an effective probe for the itinerant spinons in the QSL candidates [7, 25–27, 39]. However, in most of these materials, there are rather strong coupling between phonons and spinons, which leads to the odd temperature dependence of ultralow-temperature κ . As a result, some QSL candidates exhibit weak temperature dependence of phonon thermal conductivity and rather small κ_0/T contributed by the spinon transport. In this sense, although $\text{PrMgAl}_{11}\text{O}_{19}$ displays negligible κ_0/T at zero field, the κ data actually indicates the existence of gapless spinons that scatter with phonons. The strong recovery of κ at high magnetic fields along the c axis indeed demonstrates such kind of scattering effect at zero field. The peculiar phenomenon found in this work is that the a -axis magnetic field affects the κ very weakly, in contrast to the case of applying c -axis magnetic field. As discussed above, this can be understood based on the Ising-like anisotropy of $\text{PrMgAl}_{11}\text{O}_{19}$. At present, the Ising-type QSL candidates are very rare and the relevant physics needs further investigations.

V. SUMMARY

We have successfully grown centimeter-sized single crystal of a perfect triangular-lattice compound $\text{PrMgAl}_{11}\text{O}_{19}$ by using the optical floating-zone technique. The magnetic susceptibility reveals Ising-like interactions with antiferromagnetic correlations between Pr^{3+} ions. Both specific heat and thermal conductivity measurements reveal the absence of long-range magnetic order down to several tens of milliKelvin. Furthermore, the zero-field $C_p(T)$ curve exhibits power-law T -dependent behavior at low temperatures, reminiscent of the gapless magnetic excitations in QSL. The temperature and magnetic field dependencies of ultralow-temperature thermal conductivity suggest that there are gapless spinons scattering with phonons rather than transporting heat.

ACKNOWLEDGMENTS

This work was supported by the National Key Research and Development Program of China (Grant No. 2023YFA1406500), the National Natural Science Foundation of China (Grant Nos. 12274388, 12104010, 12104011, and 12075205) and the Nature Science Foundation of Anhui Province (Grant Nos. 1908085MA09 and 2108085QA22). The work at the University of Tennessee was supported by the NSF with Grant No. NSF-DMR-2003117. H.W. and W.X. are supported by the U.S. DOE-BES under Contract No. DE-SC0023648.

-
- [1] R. Moessner and A. P. Ramirez, Geometrical frustration, *Phys. Today* **59**, 24 (2006).
 - [2] L. Balents, Spin liquids in frustrated magnets, *Nature* **464**, 199 (2010).
 - [3] Y. Zhou, K. Kanoda, and T.-K. Ng, Quantum spin liquid states, *Rev. Mod. Phys.* **89**, 025003 (2017).
 - [4] J. Knolle and R. Moessner, A field guide to spin liquids, *Annu. Rev. Condens. Matter Phys.* **10**, 451 (2019).
 - [5] P. W. Anderson, Resonating valence bonds: A new kind of insulator? *Mater. Res. Bull.* **8**, 153 (1973).
 - [6] B. Miksch, A. Pustogow, M. J. Rahim, A. A. Bardin, K. Kanoda, J. A. Schlueter, R. Hübner, M. Scheffler, and M. Dresse, Gapped magnetic ground state in quantum spin liquid candidate κ -(BEDT-TTF)₂Cu₂(CN)₃, *Science* **372**, 276 (2021).
 - [7] M. Yamashita, N. Nakata, Y. Senshu, M. Nagata, H. M. Yamamoto, R. Kato, T. Shibauchi, and Y. Matsuda, Highly mobile gapless excitations in a two-dimensional candidate quantum spin liquid, *Science* **328**, 1246 (2010).
 - [8] Y. Li, H. Liao, Z. Zhang, S. Li, F. Jin, L. Ling, L. Zhang, Y. Zou, L. Pi, Z. Yang, J. Wang, Z. Wu, and Q. Zhang, Gapless quantum spin liquid ground state in the two-dimensional spin-1/2 triangular antiferromagnet YbMgGaO_4 , *Sci. Rep.* **5**, 16419 (2015).
 - [9] W. Liu, Z. Zhang, J. Ji, Y. Liu, J. Li, X. Wang, H. Lei, G. Chen, and Q. Zhang, Rare-earth chalcogenides: A large family of triangular lattice spin liquid candidates, *Chin. Phys. Lett.* **35**, 117501 (2018).
 - [10] R. Zhang, S. Guo, G. Xu, Z. Xu, and R. J. Cava, Strong quantum fluctuations in a quantum spin liquid candidate with a Co-based triangular lattice, *Proc. Natl. Acad. Sci. USA* **116**, 14505 (2019).
 - [11] M. Ashtar, Y. X. Gao, C. L. Wang, Y. Qiu, W. Tong, Y. M. Zou, X. W. Zhang, M. A. Marwat, S. L. Yuan, and Z. M. Tian, Synthesis, structure and magnetic properties of rare-earth $\text{RE}\text{MgAl}_{11}\text{O}_{19}$ ($\text{RE} = \text{Pr}, \text{Nd}$) compounds with two-dimensional triangular lattice, *J. Alloys Compd.* **802**, 146 (2019).
 - [12] M. Ashtar, M. A. Marwat, Y. X. Gao, Z. T. Zhang, L. Pi, S. L. Yuan, and Z. M. Tian, $\text{REZnAl}_{11}\text{O}_{19}$ ($\text{RE} = \text{Pr}, \text{Nd}, \text{Sm-Tb}$): a new family of ideal 2D triangular lattice frustrated magnets, *J. Mater. Chem. C* **7**, 10073 (2019).
 - [13] T. Arh, B. Sana, M. Pregelj, P. Khuntia, Z. Jagličić, M. D. Le, P. K. Biswas, P. Manuel, L. Mangin-Thro, A. Ozarowski and A. Zorko, The Ising triangular-lattice antiferromagnet neodymium heptatantalate as a quantum spin liquid candidate, *Nat. Mater.* **21**, 416 (2022).
 - [14] F. Song, A. Liu, Q. Chen, J. Zhou, J. Li, W. Tong, S. Wang, Y. Wang, H. Lu, S. Yuan, H. Guo, and Z. Tian,

- $\text{Ba}_6\text{RE}_2\text{Ti}_4\text{O}_{17}$ ($\text{RE} = \text{Nd, Sm, Gd, Dy-Yb}$): A family of quasi-two-dimensional triangular lattice magnets, arXiv:2311.08937 (2023).
- [15] S. Xu, R. Bag, N. E. Sherman, L. Yadav, A. I. Kolesnikov, A. A. Podlesnyak, J. E. Moore, and S. Haravifard, Realization of U(1) Dirac quantum spin liquid in $\text{YbZn}_2\text{GaO}_5$, arXiv:2305.20040 (2023).
 - [16] B. R. Ortiz, P. M. Sarte, A. H. Avidor, A. Hay, E. Kenney, A. I. Kolesnikov, D. M. Pajerowski, A. A. Aczel, K. M. Taddei, C. M. Brown, C. Wang, M. J. Graf, R. Seshadri, L. Balents, and S. D. Wilson, Quantum disordered ground state in the triangular-lattice magnet NaRuO_2 , Nat. Phys. **19**, 943 (2023).
 - [17] L. Clark, G. Sala, D. D. Maharaj, M. B. Stone, K. S. Knight, M. T. F. Telling, X. Wang, X. Xu, J. Kim, Y. Li, S.-W. Cheong, and B. D. Gaulin, Two-dimensional spin liquid behaviour in the triangular-honeycomb antiferromagnet TbInO_3 , Nat. Phys. **15**, 262 (2019).
 - [18] D. E. Freedman, T. H. Han, A. Prodi, P. Müller, Q.-Z. Huang, Y.-S. Chen, S. M. Webb, Y. S. Lee, T. M. McQueen, and D. G. Nocera, Site Specific X-ray Anomalous Dispersion of the Geometrically Frustrated Kagomé Magnet, Herbertsmithite, $\text{ZnCu}_3(\text{OH})_6\text{Cl}_2$, J. Am. Chem. Soc. **132**, 16185 (2010).
 - [19] M. R. Norman, Colloquium: Herbertsmithite and the search for the quantum spin liquid, Rev. Mod. Phys. **88**, 041002 (2016).
 - [20] Y. Shen, Y.-D. Li, H. Wo, Y. Li, S. Shen, B. Pan, Q. Wang, H. C. Walker, P. Steffens, M. Boehm, Y. Hao, D. L. Quintero-Castro, L. W. Harriger, M. D. Frontzek, L. Hao, S. Meng, Q. Zhang, G. Chen, and J. Zhao, Evidence for a spinon Fermi surface in a triangular-lattice quantum-spin-liquid candidate, Nature **540**, 559 (2016).
 - [21] Y. Li, D. Adroja, P. K. Biswas, P. J. Baker, Q. Zhang, J. Liu, A. A. Tsirlin, P. Gegenwart, and Q. Zhang, Muon Spin Relaxation Evidence for the U(1) Quantum Spin-Liquid Ground State in the Triangular Antiferromagnet YbMgGaO_4 , Phys. Rev. Lett. **117**, 097201 (2016).
 - [22] Z. Zhu, P. A. Maksimov, S. R. White, and A. L. Chernyshev, Disorder-Induced Mimicry of a Spin Liquid in YbMgGaO_4 , Phys. Rev. Lett. **119**, 157201 (2017).
 - [23] Z. Ma, S. Zheng, Y. Chen, R. Xu, Z.-Y. Dong, J. Wang, H. Du, J. P. Embs, S. Li, Y. Li, Y. Zhang, M. Liu, R. Zhong, J.-M. Liu, and J. Wen, Possible gapless quantum spin liquid behavior in the triangular-lattice Ising antiferromagnet $\text{PrMgAl}_{11}\text{O}_{19}$, Phys. Rev. B **109**, 165143 (2024).
 - [24] H. Bu, M. Ashtar, T. Shiroka, H. C. Walker, Z. Fu, J. Zhao, J. S. Gardner, G. Chen, Z. Tian, and H. Guo, Gapless triangular-lattice spin-liquid candidate $\text{PrZnAl}_{11}\text{O}_{19}$, Phys. Rev. B **106**, 134428 (2022).
 - [25] S. Guang, N. Li, R. L. Luo, Q. Huang, Y. Wang, X. Yue, K. Xia, Q. Li, X. Zhao, G. Chen, H. Zhou, and X. Sun, Thermal transport of fractionalized antiferromagnetic and field-induced states in the Kitaev material $\text{Na}_2\text{Co}_2\text{TeO}_6$, Phys. Rev. B **107**, 184423 (2023).
 - [26] X. Rao, G. Hussain, Q. Huang, W. J. Chu, N. Li, X. Zhao, Z. Dun, E. S. Choi, T. Asaba, L. Chen, L. Li, X. Y. Yue, N. N. Wang, J.-G. Cheng, Y. H. Gao, Y. Shen, J. Zhao, G. Chen, H. D. Zhou, and X. F. Sun, Survival of itinerant excitations and quantum spin state transitions in YbMgGaO_4 with chemical disorder, Nat. Commun. **12**, 4949 (2021).
 - [27] N. Li, Q. Huang, X. Y. Yue, W. J. Chu, Q. Chen, E. S. Choi, X. Zhao, H. D. Zhou, and X. F. Sun, Possible itinerant excitations and quantum spin state transitions in the effective spin-1/2 triangular-lattice antiferromagnet $\text{Na}_2\text{BaCo}(\text{PO}_4)_2$, Nat. Commun. **11**, 4216 (2020).
 - [28] S. Zheng, H. Wo, Y. Gu, R. L. Luo, Y. Gu, Y. Zhu, P. Steffens, M. Boehm, Q. Wang, G. Chen, and J. Zhao, Exchange-renormalized crystal field excitations in the quantum Ising magnet KTmSe_2 , Phys. Rev. B **108**, 054435 (2023).
 - [29] J. Xing, L. D. Sanjeewa, J. Kim, W. R. Meier, A. F. May, Q. Zheng, R. Custelcean, G. R. Stewart, and A. S. Sefat, Synthesis, magnetization, and heat capacity of triangular lattice materials NaErSe_2 and KErSe_2 , Phys. Rev. Materials **3**, 114413 (2019).
 - [30] W. Liu, Z. Zhang, D. Yan, J. Li, Z. Zhang, J. Ji, F. Jin, Y. Shi, and Q. Zhang, Effects of the Crystalline Electric Field in the KErTe_2 Quantum Spin Liquid Candidate, arXiv:2108.09693 (2021).
 - [31] Q. J. Li, Z. Y. Zhao, C. Fan, F. B. Zhang, H. D. Zhou, X. Zhao, and X. F. Sun, Phonon-glass-like behavior of magnetic origin in single-crystal $\text{Tb}_2\text{Ti}_2\text{O}_7$, Phys. Rev. B **87**, 214408 (2013).
 - [32] Z. Zeng, X. Ma, S. Wu, H.-F. Li, Z. Tao, X. Lu, X.-h. Chen, J.-X. Mi, S.-J. Song, G.-H. Cao, G. Che, K. Li, G. Li, H. Luo, Z. Y. Meng, and S. Li, Possible Dirac quantum spin liquid in the kagome quantum antiferromagnet $\text{YCu}_3(\text{OH})_6\text{Br}_2[\text{Br}_x(\text{OH})_{1-x}]$, Phys. Rev. B **105**, L121109 (2022).
 - [33] J. S. Helton, K. Matan, M. P. Shores, E. A. Nytko, B. M. Bartlett, Y. Yoshida, Y. Takano, A. Suslov, Y. Qiu, J.-H. Chung, D. G. Nocera, and Y. S. Lee, Spin Dynamics of the Spin-1/2 Kagome Lattice Antiferromagnet $\text{ZnCu}_3(\text{OH})_6\text{Cl}_2$, Phys. Rev. Lett. **98**, 107204 (2007).
 - [34] S. Jeon, D. Wulferding, Y. Choi, S. Lee, K. Nam, K. H. Kim, M. Lee, T.-H. Jang, J.-H. Park, S. Lee, S. Choi, C. Lee, H. Nojiri, and K.-Y. Choi, One-ninth magnetization plateau stabilized by spin entanglement in a kagome antiferromagnet, Nat. Phys. **20**, 435 (2024).
 - [35] A. Tari, *Specific Heat of Matter at Low Temperatures* (Imperial College Press, 2003).
 - [36] Z. Y. Zhao, X. M. Wang, C. Fan, W. Tao, X. G. Liu, W. P. Ke, F. B. Zhang, X. Zhao, and X. F. Sun, Magnetic phase transitions and magnetoelectric coupling of GdFe_3 single crystals probed by low-temperature heat transport, Phys. Rev. B **83**, 014414 (2011).
 - [37] R. Berman, Thermal Conduction in Solids (Oxford University Press, Oxford, 1976).
 - [38] X. F. Sun and Y. Ando, Comment on “Low-temperature phonon thermal conductivity of single-crystalline Nd_2CuO_4 : Effects of sample size and surface roughness”, Phys. Rev. B **79**, 176501 (2009).
 - [39] H. Murayama, Y. Sato, T. Taniguchi, R. Kurihara, X. Z. Xing, W. Huang, S. Kasahara, Y. Kasahara, I. Kimchi, M. Yoshida, Y. Iwasa, Y. Mizukami, T. Shibauchi, M. Konczykowski, and Y. Matsuda, Effect of quenched disorder on the quantum spin liquid state of the triangular-lattice antiferromagnet $1T\text{-TaS}_2$, Phys. Rev. Research **2**, 013099 (2022).